Dynamically constrained projection for subsurface current velocity

Colin Y. Shen and Thomas E. Evans
Naval Research Laboratory, Washington, District of Columbia, USA

Received 22 June 2001; revised 3 June 2002; accepted 24 June 2002; published 22 November 2002.

[1] An approach is described that projects surface current observations downward to obtain subsurface current structure consistent with the interior current dynamics. The projection approach is unrestricted by water depth. However, this study emphasizes well-mixed constant density flow in water depths appropriate for mid and outer shelf, where viscous and inertial processes are comparably important. By means of twin experiments, in which the projected current profiles are compared to the known simulated current profiles, it is shown that both the projection time step and the time domain affect the accuracy of the projection. At minimum, the time domain needs to span the dominant period of current oscillation while the time step resolves this oscillation. When both are achieved, the projected current profiles converge to the simulated profiles, and this convergence can be faster than that by assimilating surface observations to correct model spin-up from an inaccurately known initial condition. Furthermore, the projection is shown to be robust in the presence of data noise, and with appropriate weighting of the data constraints, the effect of noise on the projection accuracy can be minimized. In the present projection problem, the sea surface slope is assumed unknown and obtained together with the current profile. The use of variable eddy viscosity in velocity projection is illustrated as well with an iterative procedure. *INDEX TERMS:* 4255 Oceanography: General: Numerical modeling; 4512 Oceanography: Physical: Currents; 4219 Oceanography: General: Continental shelf processes; *KEYWORDS:* velocity projection, data assimilation, coastal current, HF radar, nowcast

Citation: Shen, C. Y., and T. E. Evans, Dynamically constrained projection for subsurface current velocity, *J. Geophys. Res.*, *107*(C11), 3203, doi:10.1029/2001JC001036, 2002.

1. Introduction

[2] This study is concerned with the estimation of subsurface coastal current structure using surface current observations. There has been a growing interest in this problem since the advent of coastal high frequency (HF) Doppler radars has made continuous synoptic observations of coastal surface currents feasible. This use of HF radars for coastal studies is now well documented in the literature [e.g., *Prandle*, 1991; *Shay et al.*, 1995; *Paduan and Rosenfeld*, 1996]. Motivated by such observations, some efforts have begun recently to develop subsurface estimation procedures [*Lewis et al.*, 1998; *Scott et al.*, 2000] based on the data assimilation approach in which the surface current data are used to update coastal ocean model solutions.

[3] A separate effort was made recently to use the surface current data to directly estimate the subsurface current structure [*Shen and Evans*, 2001], as opposed to assimilating the data into the model calculation. Their work takes advantage of the viscous coupling between the surface and subsurface motion in shallow coastal waters to relate the surface current velocity and shear to the variation of subsurface velocity with depth; the coupling is deduced from the downward momentum diffusion in the surface momentum balance equations and is resolved by orthogonal modes spanning the water column. The method is shown to be applicable to the shallow water, but its reliance on viscous coupling limits the inference to depth $< \sim 50$ m where the surface and bottom viscous Ekman boundary layers overlap.

[4] The present study seeks an estimation approach that expands the use of the momentum balance equations to the whole water column and obtains subsurface current estimates consistent with this interior momentum balance, rather than relying on the near surface balance and viscous coupling. With this approach, by using the momentum balance at all depths, both the inertial and viscous effects can be accounted for, and this in turn should make it possible to extend the estimation beyond viscous shallow waters into deeper coastal waters, where both effects contribute to the variation of current velocity with depth. The estimation approach to be presented will be referred to as "velocity projection" as in the previous study, since the idea remains that of using surface current observation to estimate downward the subsurface current structure. However, it will be seen that the formulation undertaken here does not excluded the use of subsurface observations, such as moored current meter measurements, when they are available.

[5] The present interest is still the coastal setting considered previously, and the same homogenous shallow water current model will be used, in which winds and tides are the primary forcing, and the water density is constant and well mixed. The investigation with this model, however, will be

0148-0227/02/2001JC001036$09.00

limited to the linear flow regime, for which the uniqueness of the projection solution can be assured. This is important for obtaining physically meaningful estimates as well as an important step toward estimation with nonlinear models, which admits multiple flow states, and the selection of the correct state may require guidance from the linear model solution. It may be noted further that in velocity projection, the surface velocity data are specified at all projection time steps, which is feasible with high resolution time series measurements such as those available from HF radars. Thus, at each step with suitable weighting of the data and model constraints, it should be possible to keep the model errors in check, in particular, the omitted nonlinearity, in which case the dense temporal data coverage in effect help keep the linear model on "track" [*Wunsch*, 1990].

[6] The usefulness of the estimation approach developed here ultimately has to be tested by comparing it against observations. However, without an a priori understanding of the method's capabilities and limitations, such comparisons run the risk of yielding possibly erroneous conclusions. Therefore, the following issues will be addressed specifically in this study: (1) The accuracy limit of velocity projection for observations of finite duration and temporal resolution; (2) the vertical resolution achievable by the projection estimation of subsurface current; (3) the effect of data noise on the projection estimation; and (4) the accuracy of velocity projection versus that of model spin-up and data assimilation beginning from an assumed initial condition. These issues will be addressed using the twin-experiment approach, in which the shallow water momentum equations used for velocity projection are integrated in time with prescribed wind and tidal forcing to generate a simulated current field; then, downward velocity projection is made using the simulated surface current velocities as input, and results compared with simulated current profiles. This should allow an unambiguous determination of the method's accuracy limits and, thereby, should provide the necessary groundwork for applications of the method to real data. Coastal regions suitable for the application of the present method will be those dominated by winds and tides and negligibly affected by baroclinic forcing.

[7] This paper is organized as follows: In section 2, the tidally/wind driven, linearized shallow water model is described. The two main model assumptions are that (1) baroclinic effect is negligible, and (2) the vertical viscous stress is the dominant frictional force in the coastal water. The velocity projection using this model requires only the local surface wind stress and current velocity as input. The sea surface slope due to tides is not needed for the projection but is deduced from the model as part of the projection. In section 3, the velocity projection approach is described, and its relation to data assimilation is discussed. In section 4, the numerical simulation that provides the reference current for evaluating the projection accuracy is described. In section 5, the velocity projection results are presented, and their accuracy is evaluated with respect to data resolution, coverage, and noise. The accuracy is also compared to that of the model forecast started from an uncertain initial condition but updated continuously via assimilation of the surface velocity data. In section 6, the summary is given.

2. Shallow Water Model

2.1. Governing Equations

[8] In well-mixed shallow water, the large-scale tidal and wind-driven currents are dissipated primarily through vertical turbulent shear stress and energy loss to the seabed. In this case, the evolution of shallow water current momentum, for the linear system considered here, is described by

$$\frac{\partial}{\partial t}(u, v) + f(-v, u) = -g\left(\frac{\partial \eta}{\partial x}, \frac{\partial \eta}{\partial y}\right) + \frac{\partial}{\partial z}\nu_e \frac{\partial}{\partial z}(u, v) \quad (1)$$

where u and v are the horizontal velocity vector components along the Cartesian x and y coordinates, respectively; η is the sea surface height; t is time; ν_e is the eddy viscosity parameterizing the vertical turbulent dissipative process; the vertical z-coordinate points positive upward; the remaining two parameters, f and g, are the Coriolis frequency and gravitational constant, respectively.

[9] It will be convenient to use a compact dimensionless representation of (1), by defining a complex velocity, $U = u + iv$ and scaling the velocity variables by U_o, t by 1/f, and z by $H = (\eta + h)/2$, where h is the bottom depth, as well as to rescale the range of local water depth to ± 1 with $+1$ at the surface and -1 at the bottom. After the nondimensionalization (henceforth all variables are dimensionless unless noted otherwise) and in terms of the complex U, (1) becomes

$$\frac{\partial U}{\partial t} + iU = -R + E\frac{\partial^2 U}{\partial z^2} \quad (2)$$

where $R = (g/fU_o)(\partial\eta/\partial x + i\partial\eta/\partial y)$is the dimensionless complex pressure gradient; $E = \delta^2/2H^2$ with the Ekman layer depth scale, $\delta = (2\nu_e/f)^{1/2}$. Here, ν_e has been assumed to be uniform with respect to depth. The velocity projection approach described in this paper applies equally to depth-dependent ν_e. The complication is the dependence of ν_e on the current strength. This is considered later with a simple eddy viscosity model in which ν_e varies in time with the kinetic energy of the mean flow. In using (2) for velocity projection, R can either be given by the radar altimeter measurement of sea surface height or be treated as an unknown variable to be determined as part of the velocity projection. This is discussed in section 3.

2.2. Boundary Conditions

[10] The formal mathematical solution of (2) with R given requires two boundary conditions on U as well as the starting values of U at a specified time. Typically, in ocean models the surface boundary condition is the wind stress $\tau(= \tau_x + i\tau_y)$, which is related to vertical shear, in dimensionless unit, by

$$\left.\frac{\partial U}{\partial z}\right|_{z=1} = \tau \quad (3a)$$

with τ scaled by $\nu_e U_o/H$. The bottom boundary condition can be either a velocity dependent stress at some small height above the bottom or zero velocity at the seabed. Here, for the velocity projection, the surface boundary condition will still be (3a), while the condition to be used at the bottom will be that of no slip, that is,

$$U|_{z=-1} = 0. \quad (3b)$$

This simpler boundary condition is also preferred for another reason to be noted shortly. But, if needed, the stress bottom boundary condition can be used instead of (3b) or even together with (3b). In the latter case, one of them is to be treated as an auxiliary condition as described below.

[11] Velocity projection considered here differs from the conventional forward time integration in that auxiliary boundary conditions can be specified in place of the initial condition, which may not be known. A time series of surface velocity vectors,

$$U|_{z=1} = U\eta(t) \tag{4a}$$

such as that obtainable with HF radar, clearly represents an auxiliary boundary condition once (3a) and (3b) are specified. Other types of current measurements, not at the sea surface, can also be incorporated into velocity projection as auxiliary boundary conditions; for example, velocity time series measured by a subsurface moored current meter, or the velocity cross section of a current field measured by an acoustic tomographic array. Moreover, using the available boundary conditions such as (3a), (3b), and (4a), it is possible to generate additional auxiliary dynamic boundary conditions from the momentum equations as shown by *Shen and Evans* [2001]. For the sake of clarity, however, the present study will be limited to only two auxiliary boundary constraints, namely, (4a) and

$$E\frac{\partial^2 U}{\partial z^2}|_{z=-1} = R \tag{4b}$$

obtained by applying the no-slip condition (3b) to the momentum balance (2) at seabed. The use of this bottom dynamic boundary condition conveniently eliminates the need for the sea surface slope data in velocity projection as will be seen in section 3.

2.3. Modal Approximation

[12] Let $F_n(z)$, n = 0, 1, 2,...∞, be the complete set of orthonormal functions spanning the local water depth, so that at a given horizontal position,

$$U(z,t) = \sum_{n=0}^{\infty} \alpha_n(t) F_n(z) \tag{5}$$

where $\alpha_n(t)$ is complex. For definitiveness, $F_n(z)$ will be assumed to be the Chebyshev polynomials (other basis functions are equally feasible) with the following orthonormal properties,

$$\int_{-1}^{1} \alpha(z) F_j(z) F_n(z) dz = \begin{cases} c_{jn}, & j = n \\ 0, & j \neq n \end{cases} \tag{6}$$

where the weight, $\sigma(z) = (1 - z^2)^{-1/2}$ and $c_{00} = \pi$; otherwise, $c_{jj} = \pi/2$.

[13] Let $\tilde{U}$ be the approximation of U given by the first N terms of the expansion (5),

$$\tilde{U}(x,t) = \sum_{n=0}^{N-1} \alpha_n(t) F_n(z) \tag{7}$$

with N chosen such that $|\tilde{U}| \gg |U - \tilde{U}|$.

[14] The problem of estimating U now becomes one of determining the time dependent coefficients α_n. The surface and bottom boundary conditions (3a) and (3b) imply the following relationships between the α_n's,

$$\left.\frac{\partial \tilde{U}}{\partial z}\right|_{z=1} = \sum_{n=0}^{N-1} n^2 \alpha_n \cong \tau \tag{8a}$$

$$\sum_{n=0}^{N-1} (-1)^n \alpha_n \cong 0 \tag{8b}$$

[15] The momentum equation (2) provides another set of relationships between α_n's, after substituting (7) into (2) and applying the orthonormal condition (6):

$$c_{jj}\left(\frac{\partial \alpha_j}{\partial t} + i\alpha_j\right) = -c_{0j}R + E\sum_{n=2}^{N-1} \alpha_n \left(\int_{-1}^{1} \alpha F_j \frac{\partial^2 F_n}{\partial z^2} dz\right),$$
$$j = 0, 1, 2, \ldots, N-3 \tag{9}$$

The modal equations for the two highest coefficients α_{N-2} and α_{N-1} are omitted. These two coefficients are to be obtained from the boundary conditions (8a) and (8b). This is, in essence, the "tau" approximation in the finite-dimensional spectral representation of a differential equation and its boundary conditions [*Lanzcos*, 1956]. In the presence of the auxiliary boundary conditions, which are now

$$\sum_{n=0}^{N-1} \alpha_n \cong U_\eta, \tag{10a}$$

and

$$E\sum_{n=2}^{N-1} \alpha_n \left.\frac{\partial^2 F_n}{\partial z^2}\right|_{-1} \cong R, \tag{10b}$$

an additional α_{N-3} modal equation can be dropped from (9) on account of (10b). In the context of the tau approximation, (7) thus may be viewed explicitly as the sum of two parts

$$\tilde{U} = \sum_{n=0}^{N-4} \alpha_n F_n(z) + \sum_{n=N-3}^{N-1} \alpha_n F_n(z)$$

with the last summation appended to satisfy all the boundary conditions except (10a).

3. Velocity Projection

[16] When there are N modes and M boundary conditions, K = N − M + 1 consecutive observations in time are needed to determine the unknown modal amplitudes. The following discretization of (8a)–(10a) makes this requirement clear: Let the superscripts (k) be the index for time, t_k. (8a), (8b), (10a), and (10b) at each t_k are

$$\sum_{n=0}^{N-1} n^2 \alpha_n^{(k)} \cong \tau^{(k)}, \tag{11a}$$

$$\sum_{n=0}^{N-1}(-1)^n\alpha_n^{(k)} \cong 0, \tag{11b}$$

$$\sum_{n=0}^{N-1}\alpha_n^{(k)} \cong U_\eta^k, \tag{11c}$$

$$E\sum_{n=0}^{N-1}\alpha_n^{(k)}\frac{\partial^2 F_n}{\partial z^2}\Big|_{-1} \cong R^k. \tag{11d}$$

Equation (9), discretized in time using the trapezoidal rule and after the rearrangement of the terms, is

$$\sum_{n=0}^{N-1}\left[c_{jj}\left(-1+\frac{i}{2}\Delta t\right)\delta_{jn}-\Delta t G_{jn}\right]\alpha_n^{(k)} + \left[c_{jj}\left(1+\frac{i}{2}\Delta t\right)\delta_{jn}-\Delta t G_{jn}\right]\alpha_n^{(k+1)} = -\frac{c_{0j}}{2}\Delta t\left(R^{(k+1)}+R^{(k)}\right), j=0,1,2,\ldots,N-4 \tag{11e}$$

where

$$G_{jn}=\begin{cases}0, & n=0,1\\ E\int_{-1}^{1}\sigma F_j\frac{\partial^2 F_n}{\partial z^2}dz, & n>2\end{cases}.$$

[17] In the present problem, M = 4. Suppose that N = 5. Then, as already noted, K = N − M + 1, or surface data at two times, and, (K = 2) are needed to determine α_n. This is easily verified to be the case: At these two times, there are a total of 10 unknown α_n's. But, there are 8 boundary constraints (11a)–(11d) and 2 dynamic constraints (11e) between two times. Hence, the total number of unknown equals to the number of constraints, and α_n's are exactly determined. In the same manner, it can be verified that each time a higher mode is added, one additional observation in time is required to uniquely determine α_n's.

[18] In practice, N is chosen a priori and fixed, while the data is continuously collected. Hence, typically, K > N − M + 1, and (11a–11d) constitute an overdetermined system. This outcome is, in fact, what is needed to deal with actual data which are invariably noisy. The effect of noisy data on projection is discussed in section 5.4.

[19] The projection trivially becomes assimilation when the current structure is known approximately at t_1, and a forecast at the subsequent time steps is to be found that best fits the surface data, boundary conditions, and the initial value at t_1. This can be seen readily by appending the initial conditions,

$$\alpha_n^{(1)} = d_n, \quad n=0,1,2,\ldots,N-1 \tag{11f}$$

to (11a–11d), where d_n is the given initial value. This renders the whole system, which now includes (11f), overdetermined for any K > 1. Formally, the problem of finding the best fit can be posed as minimizing the "cost" function, which is the weighted sum of the squares of the differences between the "solution" on the left-hand side and the "data" on the right-hand side of (11a)–(11f) for all k = 1, 2,. . ., K. The reader is referred to, e.g., *Wunsch* [1996] for the various cost function minimization methods.

[20] For the present model, with z being the only relevant space dimension, the size of the system of linear equations (11a)–(11f) is quite manageable from the point of view of direct matrix inversion. The method of singular value decomposition is the method of choice in this case for obtaining the least squares solution, and is used in the following to obtain all the velocity projection results and the accompanying data assimilation results.

[21] The sea surface height gradient needed to calculate R at the HF radar resolution of km and minutes is difficult to obtain with confidence from either remote sensing or direct sea surface height measurements, since to obtain the typical sea surface height gradient of 10^{-5} to 10^{-6} on the scales of the HF radar resolution would require an accuracy of <0.1 cm in the height measurement, which is not yet achievable with existing technology. Given that the surface height gradient needed to calculate R is essentially unknown, the constraint (11d) may be subtracted from (11e) to eliminate R, and this yields

$$\sum_{n=0}^{N-1}\left[c_{jj}\left(-1+\frac{i}{2}\Delta t\right)\delta_{jn}-\Delta t G'_{jn}\right]\alpha_n^{(k)} + \left[c_{jj}\left(1+\frac{i}{2}\Delta t\right)\delta_{jn}-\Delta t G'_{jn}\right]\alpha_n^{(k+1)} = 0 \tag{12}$$

where

$$G'_{jn}=\begin{cases}0, & n=0,1\\ E\left(\int_{-1}^{1}\sigma F_j\frac{\partial^2 F_n}{\partial z^2}dz+\frac{c_{0j}}{2}\frac{\partial^2 F_n}{\partial z^2}\Big|_{z=-1}\right) & n>2\end{cases}$$

and j = 0, 1, 2,. . ., N − 3. Note that the maximum j has been increased by one to N − 3, because of the use of boundary condition (11e) in (12), which effectively eliminates (11e) and leaves only (11a)–(11c) still as independent boundary conditions. The length of time series required to exactly determine the modal amplitudes is now simply K = N − 2.

[22] All calculations for velocity projection in this paper assume that R is unknown and obtain estimates of current structure from (11a)–(11c) and (12) with K ≥ N − 2. Once U is estimated, R can be determined from (11d).

4. Reference Current Profiles

[23] The benchmark for testing the velocity projection is the time-dependent solution of (2) obtained by conventional forward time integration from a state of rest with prescribed wind and tidal forcing. The specific functional forms of the forcing used for the integration are

$$\tau = \tau_o \sin(\omega_1 t)$$

$$R = R_o[\cos(\omega_2 t) + i\sin(\omega_2 t)]$$

where R_o is set to one, $\tau_o = H/\delta$, $\omega_1 = 0.91$, and $\omega_2 = 1.82$. To give some perspective to these dimensionless numbers, let $f = 8 \times 10^{-5}$/s, $U_o = 0.25$ m/s, and $\nu_e = 0.01$ m^2/s. Then,

$R_o = 1$ is equivalent to a tidal forcing with a sea surface slope of 2×10^{-6}, $\tau_o = H/\delta$ is equivalent to a dimensional wind stress amplitude, $\nu_e U_o/\delta = 1.58 \times 10^{-4}$ m^2/s^2, $\omega_1 = 0.91$, corresponds to a wind-forcing period of 24 hours or approximately that of the diurnal onshore and offshore sea breeze, and $\omega_2 = 1.82$ corresponds to a tidal forcing period of 12 hours or approximately that of the dominant coastal semidiurnal tide.

[24] These chosen tidal and wind-forcing frequencies are approximately the maximum typically present in the coastal ocean. Because the current velocity tends to vary more rapidly with depth with increasing forcing frequency, the use of maximum forcing frequencies here permits a more demanding test of the velocity projection. The addition of lower frequency forcing, specifically, adding wind stresses with periods >1 day to the diurnal wind stress above, are not found to have a significant effect on the projection accuracy. In fact, overall, the wind effect is less a factor in velocity projection than the higher frequency semidiurnal tide. However, there can be atypical situations where the wind effect dominates such as during the passage of wind front which tends to generate rapidly varying inertial oscillations. Such cases need to be treated separately as noted in the summary section.

[25] The solution of (2) is obtained for constant $E = E_o$ and, separately, for time-varying $E = E_t$, modeled simply in terms of the square of the depth-averaged velocity similar to that given by *Shen and Evans* [2001], or

$$E_t = rE_o = b|\overline{\tilde{U}}|^2$$

Here, for convenience, E_t is assumed approximately equal to E_o on average, that is, given E_o, b is chosen such that the time averaged r is approximately unity. For the time varying E_t, an additional factor, 1/r, multiplies the right-hand side of the boundary condition (3a).

[26] In the E_o case, four different U realizations are simulated by integrating (2) separately for E = 2.0, 0.5, 0.08, and 0.02, or equivalently $\delta/h = 1.0$, 0.5, 0.2, and 0.1, respectively. Because of the slow variation of U with respect to depth at larger E_o, due to the stronger frictional damping, it is found that the larger E_o simulations generally do not provide sufficiently demanding tests of the velocity projection. The discussion of projection accuracy in the following, therefore, will be focused on the small $E_o = 0.02$ case or $\delta/h = 0.1$, which is more typical of the condition at mid or outer shelf. The test of velocity projection in the variable E case is also limited to small E_t with a mean value equal to approximately $E_o = 0.02$.

[27] The standard implicit Crank-Nicolson scheme is used to integrate (2) with δt (to distinguished it from Δt above) chosen to be 0.002. The vertical dimension is resolved by 33 grid points or 33 Chebyshev polynomials. This resolution and the time step size are more than adequate to resolve the spatial and temporal variation of the current profiles for the E = 0.02 case. The simulated current is integrated to forced-dissipative equilibrium. Examples of the velocity profiles are shown in Figure 1. For later references, the time averaged maximum current speed and the RMS value of maximum speed variability for the constant E_o case in the equilibrium state are 1.84 and 0.48, respectively, and for the variable E_t case are 1.84 and 0.43, respectively.

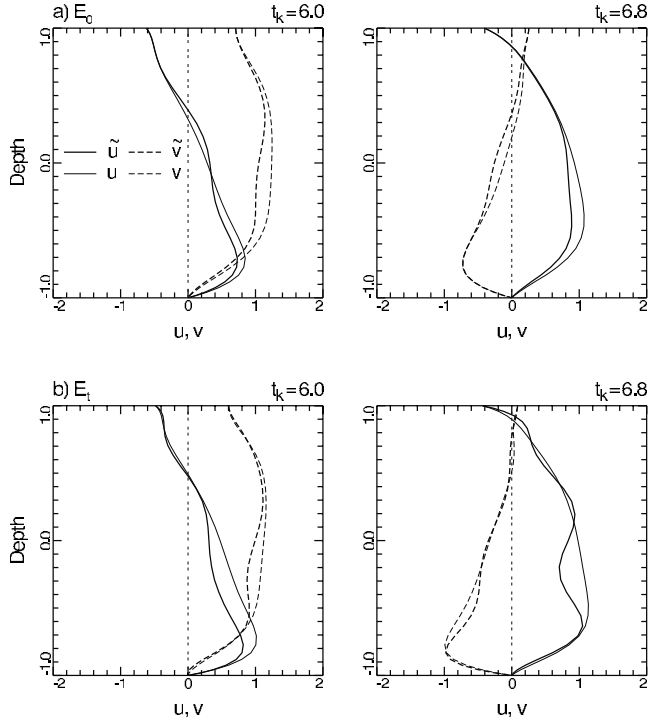

Figure 1. Examples of velocity profiles for simulated u and v and for projected ũ and ṽ. (a) Constant eddy viscosity case. (b) Variable eddy viscosity case. t_k is the dimensionless time scaled by the Coriolis frequency and measured from the beginning of a projection time domain.

5. Analysis and Discussion

[28] A number of factors affects the quality of velocity projection, in particular, the size of the sampling interval Δt, the length of the data time series, the number of vertical modes needed to resolve the current structure, and the uncertainty of the surface data. In the following, to quantify the accuracy of the projection, several measures are computed: The maximum speed difference, $|\Delta U|_{max} = |\tilde{U} - U|_{max}$, the maximum angle difference, $\Delta\theta_{max} = (\tilde{\theta} - \theta)_{max}$ (n.b. $|\Delta U|_{max}$ and $\Delta\theta_{max}$ need not occur at the same depth), and the magnitude and phase, C_r and C_θ, respectively, of the complex correlation coefficient,

$$C = \frac{\overline{\tilde{U}\tilde{U}^*}}{\overline{|\tilde{U}|}\,\overline{|\tilde{U}^*|}},$$

where the asterisk denotes complex conjugate, and the overbar denotes depth averaging.

[29] The singular value decomposition of an exactly or overdetermined system of independent constraints (11a–11c) and (12), that is, with $K \geq N - 2$, should yield formally N nonzero singular values. However, it is commonly known that the singular vectors and values calculated numerically from the decomposition are not necessarily all

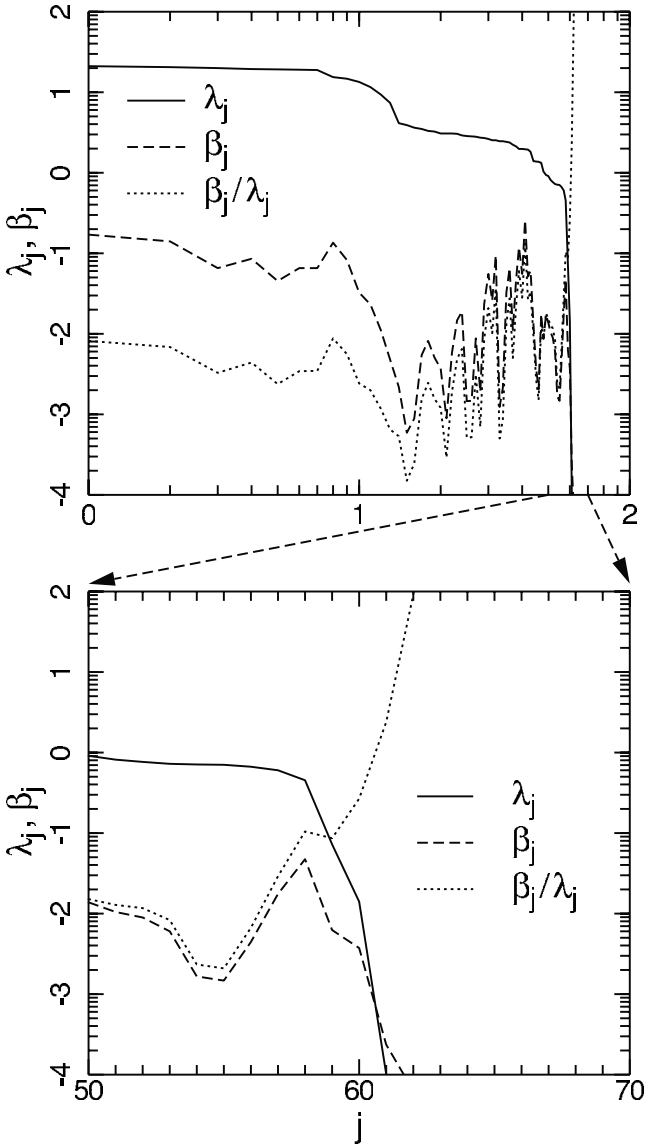

Figure 2. Examples of λ_j and β_j, respectively, the singular value and the dot product of data vector and its singular vectors. The lower panel is the plot of the spectra for $j > 50$.

usable, as the inherent inaccuracy of the calculation can render some small singular values unreliable for determining the inverse solution. Figure 2 illustrates the singular values λ_j from one such calculation (appendix A contains some other details related to singular vectors). Shown are also the dot product, β_j, of the data vector with each of its basis singular vectors, as well as the ratios, β_j/λ_j, that form the coefficients of the singular vector expansion of the solution α_n in (11a–11c) and (12). It is seen that both λ_j and β_j decrease rapidly at the high end of their respective spectrum. But, their ratio rises sharply, as λ_j becomes very small, a manifestation of the typical numerical instability at small λ_j. To avoid the distortion of the solution by such instability, the common practice is to truncate λ_j at some cutoff value. In obtaining the projection results in this study, the cutoff is set at a point where λ_j is noted to be approximately comparable to β_j and, thereafter, becomes rapidly smaller than β_j. This point is usually found four decades below the maximum λ_j or $10^{-4}(\lambda_j)_{max}$, and the adequacy of this cutoff point is confirmed by trials with smaller and larger cutoffs, say 10^{-3}, and 10^{-5}, both of which consistently produce poor results.

5.1. Projection Time Step and Domain

[30] The projection can be formulated as an exactly determined system of constraints as discussed in section 3. The solution of this system, however, does not necessarily improve with decreasing Δt as in the conventional forward time integration. The size of the time domain, ΔT also plays a role; in particular, the improvement of accuracy requires ΔT to be at least comparable to the timescale of the dominant flow. This influence of ΔT on accuracy can be seen by comparing Figure 3a to Figure 3b, which are plots of the projection errors for different Δt and, hence, different $\Delta T = (K - 1)\Delta t$ as a function of $t_k = (k - 1)\Delta t$; the errors are given in terms of the maximum ΔU and $\Delta\theta$ defined earlier; shown are also the maximum current speed $|\tilde{U}|_{max}$, the depth-averaged current speed $|\overline{\tilde{U}}|$, and the difference $|\Delta\overline{U}| = |\overline{\tilde{U}} - \overline{U}|$. In both plots, the system solved is exactly determined with $N = 9$ modes and $K = 7$ times.

[31] In the small ΔT case, Figure 3a, it is seen that the errors are unacceptably large, as $|\Delta U|_{max}$ exceeds $|\tilde{U}|_{max}$ most of the time, and $|\Delta\theta|_{max}$ fluctuates widely. This is further reflected in the low correlation coefficient C_r and the widely fluctuating phase lag C_θ. By contrast, the errors for the large ΔT case, Figure 3b, are markedly smaller, despite its four times larger Δt (=0.8). Its initially large errors are seen to decrease significantly toward the end of ΔT; especially, $|\Delta\theta|_{max}$ approaches zero. This decrease of the errors is reflected at the same time in the increase of the correlation, C_r, between the projected and reference current profiles and the decrease of the phase lag C_θ. Suppose now that ΔT of the previous $\Delta t = 0.2$ case is increased to match that of the $\Delta t = 0.8$ case; this can be accomplished by using $K = 25$, which increases ΔT to 4.8 but also renders the system overdetermined. Figure 3c shows the result of this change. One can see that there is a substantial reduction of projection errors; in fact, the errors are now essentially the same as those for the $\Delta t = 0.8$ case (Figure 3b). The larger ΔT has clearly made a difference here in determining projection accuracy.

[32] The dependence of projection accuracy on ΔT points to the importance of having adequate number of observations over a time period commensurable with the timescales of the flow. When the observational time domain, ΔT, is too small, the measurements, no matter how frequently they are made, all tend to contain similar temporal information. In this case, the actual number of independent data constraints useful for velocity projection will be less than that implied by the data, and the system may in fact be underdetermined. This is evidently the case with $\Delta T = 1.2$ (Figure 3a), which samples only about 1/4 of the tidal cycle and 1/8 of the diurnal wind cycle. However, when ΔT is increased to include as little as one tidal cycle, the flow variability in the measurements can be sufficiently large to render the velocity projection meaningful again, as it is found above in the two $\Delta T = 4.8$ cases, Figures 3b and 3c. Still more accurate projection can be obtained as ΔT is increased further in

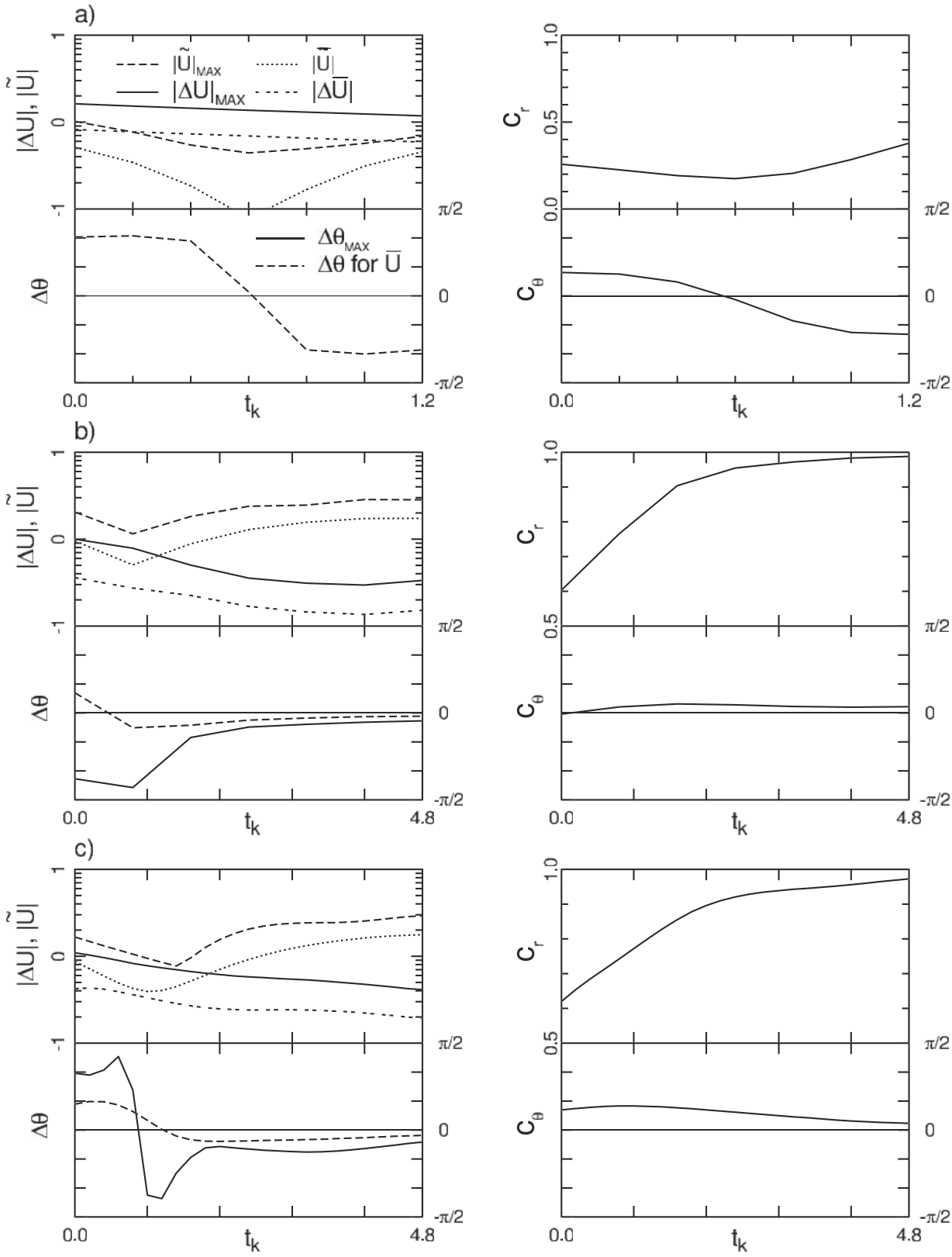

Figure 3. Projection errors, $|\Delta U|$ and $\Delta\theta$, relative to the expected current speed and direction, and the complex correlation magnitude and phase, C_r and C_θ, between the projected and expected profiles. $\tilde{U}$ and $\bar{U}$ are, respectively, the projected current speed and its depth averaged value. All current speeds are plotted on the log10 scale with the time axis denoted by t_k, where $t_k = (k-1)\Delta t$ is the time at the projection time step k, with k = 1, 2,. . .,7, for a time step size Δt. Case (a) $\Delta t = 0.2$ and time domain $\Delta T(=\max t_k) = 1.2$. Case (b) $\Delta t = 0.8$, and $\Delta T = 4.8$. Case (c) $\Delta t = 0.2$, and $\Delta T = 4.8$.

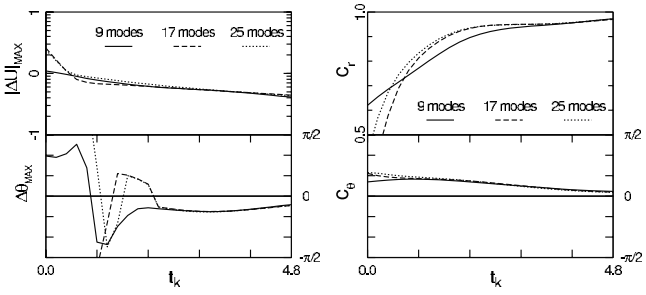

Figure 4. Comparison of maximum $|\Delta U|$ and $\Delta\theta$, and C_r and C_θ for projections using 9, 17, and 25 modes.

include more variability. At what point the optimal solution is obtained is a question taken up in section 5.3.

[33] The data dependence or independence referred to in the foregoing can be quantified with the calculation of the ''data'' resolution matrix; additionally, it is useful to identify the solution dependence or independence in the velocity projection with the calculation of the ''solution'' resolution matrix. (The details of both are left to appendix A.) The aspect of interest concerning the solution dependence is the large projection errors that consistently occur near the beginning of the time domain in Figure 3 irrespective of the sizes of ΔT and Δt. The solution resolution matrix in appendix A shows that the projection solutions earlier in ΔT depend on those later. Since the solutions across time domain are related through the time-dependent dynamic equations or constraints, this dependence implies that at least partially backward time integration of the equations is involved in determining the early time projection solutions. In a non conservative dynamic system, as it is with the present model, flow information can not be recovered accurately in backward time integration. This inaccuracy is most likely to have contributed to the consistently large error in the projection solution at early times.

5.2. Vertical Resolution

[34] Figure 4 shows the projection accuracy for increasing numbers of vertical modes used to approximate the velocity profile. The accuracy is seen to differ mostly in the early part of ΔT where errors in ΔU and $\Delta\theta$ are large and correlation is low. Beyond the mid point of ΔT, the accuracy improves; moreover, the errors become about the same size for all three resolutions and so do the correlation C_r and phase lag C_θ. As pointed out at the end of the preceding section 5.1, the projection errors are large earlier in ΔT, because the projection solutions at early times depend partly on backward time integration from the solutions at later times. In a backward integration, the higher order modes, which are more dissipative and less recoverable, are the main contributors of the errors. The larger errors for the higher resolution projection in Figure 4 near the beginning of ΔT reflect largely the greater inaccuracy of the additional higher order modes in the solutions. The higher resolution, however, is seen to improve the correlation C_r in the middle part of ΔT. The projection accuracy for all three resolutions are about the same in the second half of ΔT indicating that the 9-mode resolution is adequate for the particular flow situation considered here.

5.3. Convergence

[35] As ΔT is increased, the projection solution becomes more accurate and converges toward the true solution. The rate of this convergence is of interest, in particular, in relation to the convergence achievable with data assimilation that updates the solution of a model forecast started from some inaccurately known initial condition. In Figure 5a, the maximum projection errors for increasing $\Delta T = [(7 + 8j) - 1]\Delta t$, where $\Delta t = 0.2$ and $j = 0,1, 2,\ldots, 7$, are shown as a solid curve, denoted by vp. The projection accuracy for a particular ΔT tends to vary with different surface current realizations. The solid curve represents the mean of this variation, and the vertical bar is one standard deviation about this mean, based on 12 realizations over a tidal cycle. For comparison, the errors of two prognostic calculations that assimilate the same surface velocity data but begin with prespecified initial conditions are also shown; one of which (curve da0) assumes the state of rest as the initial condition, and the other (da1) assumes a linear initial velocity profile that matches the surface velocity and the bottom no slip conditions. The fourth curve (iv1) shows the forecast errors from the calculation with the same linear initial profile but without data assimilation. In these calculations, the time step size is the same as that for projection.

[36] Figure 5a shows that the projection errors decrease at a rate faster than that at which the forecast errors are reduced by data assimilation, and clearly without any data constraint the forecast errors (iv1) decrease little with time; the angular errors for this case are often out of range and are not shown. The primary source of error in the assimilative forecast here is the uncertainty in the initial condition. The larger the initial uncertainty, the longer it takes the solution to converge to the ''true'' solution, as this can be seen by comparing da1 to da0, which have approximately the same exponential decay rate, $\sim$0.13 for the $|\Delta U|_{max}$ error. In comparison, curve vp from velocity projection decays at a rate of $\sim$0.24, up to $\Delta T = 9$. For an assimilative forecast to achieve comparable accuracy at $\Delta T = 9$ would require at least an initial condition accurate to within 20% in $|\Delta U|_{max}$ and having a minimal initial angular error.

[37] After the velocity projection, a forecast calculation may be initiated using the velocity profile at the end of projection ΔT and then assimilates surface velocity data into the model in the subsequent forward integration. In Figure 5b, curves vp.a and vp.b show the accuracy of such forecast calculations starting from the end of projection $\Delta T = 7.6$ (K = 39) and 12.4 (K = 63), respectively. These two curves decay at about the same rate 0.09; moreover, they tend to overlap, indicating that once a reasonable accuracy is achieved, the size of ΔT matters little in the subsequent assimilative forecast. Eventually, the ΔU error reaches a minimum, $\sim$0.03 or $\sim$2% of the maximum mean speed (which is in essence the smallest error achievable with the present 9 mode approximation. Increasing the vertical resolution reduces the minimum.) This is also the minimum level eventually reached by the forecast calculations with continuous data assimilation (curves da0 and da1, continued from the previous figure), while without

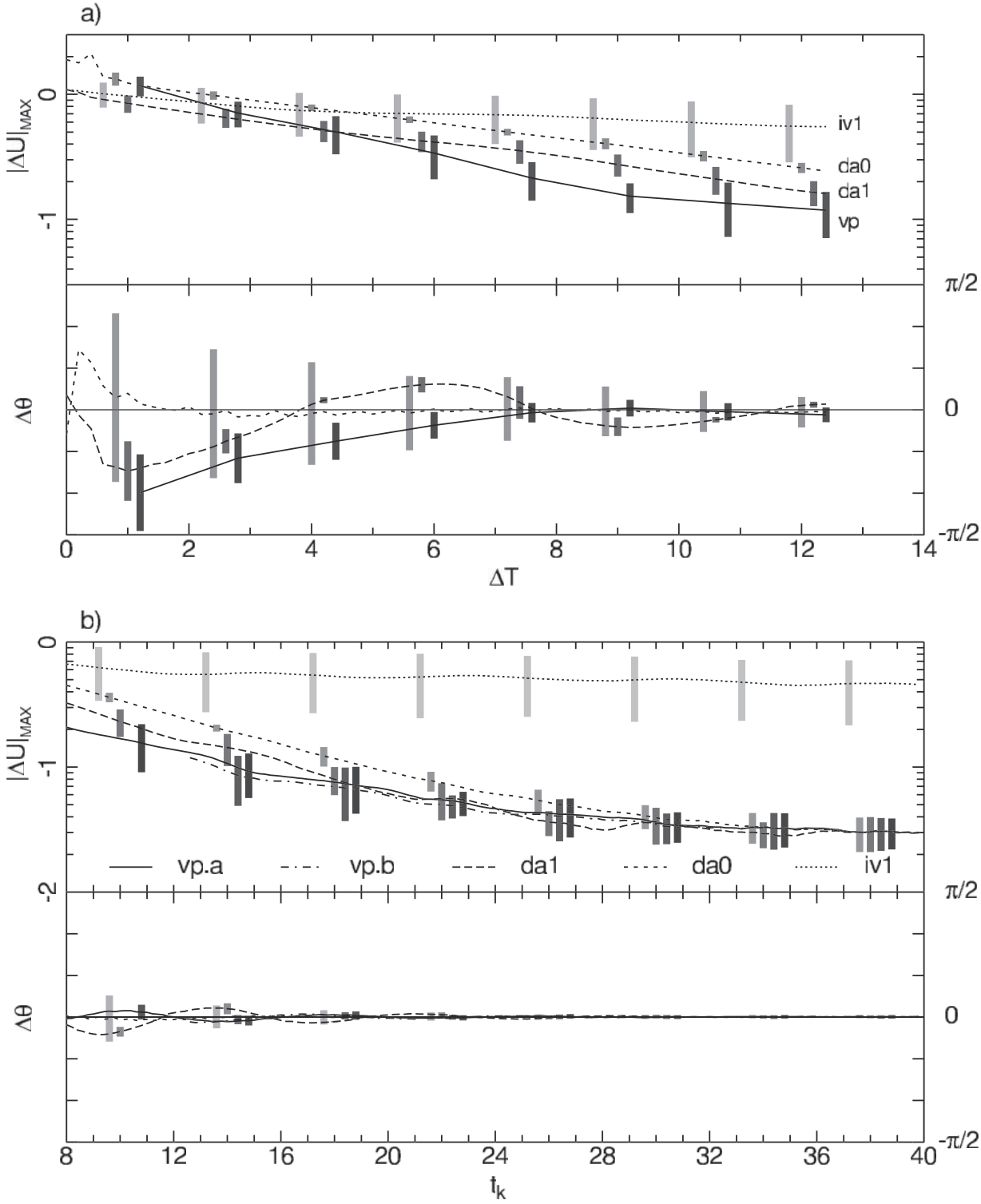

Figure 5. (a) Errors, $|\Delta U|$ and $\Delta\theta$, versus the length of the time domain, ΔT. The vertical bar is one standard deviation centered on the mean error curve. The mean error curves for the different cases are identified by vp - velocity projection, da1- data assimilation starting from linear initial velocity profile, da0 - data assimilation starting from at rest, and iv1 - no data assimilation starting from linear profile. (b) $|\Delta U|$ and $\Delta\theta$ versus time, t_k. All cases are for data assimilation. vp.a starts from the end of projection $\Delta T = 7.6$. vp.b starts from the end of projection $\Delta T = 12.4$. da1, da0, and iv1 are continuations of the curves in (a).

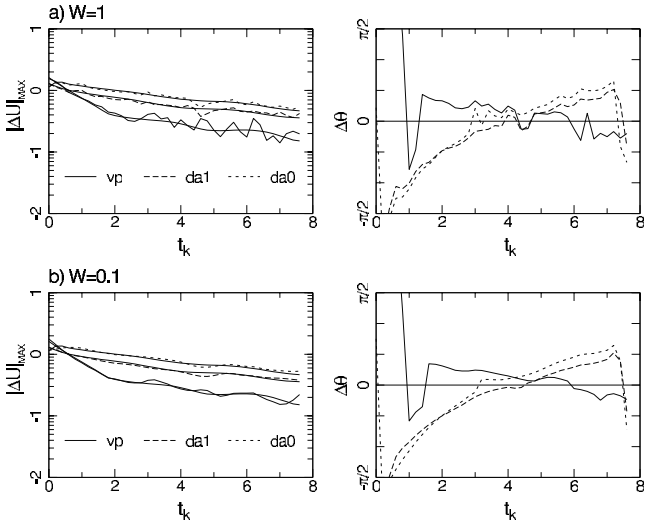

Figure 6. Effect of data noise on $|\Delta U|$ and $\Delta\theta$ errors for velocity projection (vp) and data assimilations (da1 and da0). Errors for noise free case are shown as thin solid curves. W is the weight applied to the data. (a) W = 1, normal weight. (b) W = 0.1, reduced weight.

data assimilation the errors (curve iv1) stay high. The $\Delta\theta$ errors approach zero for all the cases with data assimilation; though, the convergence to zero is more rapid for vp.a and vp.b which start from the end of projection. $\Delta\theta$ for iv1 without data assimilation does not converge and is not shown.

5.4. Data Noise

[38] The velocity projection remains robust in the presence of data noise. Figure 6 shows the accuracy of the projection made from randomly perturbed surface velocities and wind stress shears. The noise is added with the use of a random number generator; the noise amplitude added to $|U|$ is 0.012, which in dimensional unit is comparable to the uncertainty ~5 cm/s of the current velocity measured by HF radar, and the noise added to the wind stress is given an amplitude that yields approximately a surface velocity uncertainty of the same magnitude. It is customary to give a smaller weight to data constraints when the data is known to be noisy. In the present problem, the weight can be applied by multiplying (11a) and (11c) by a constant factor, W. In Figure 6, the projection errors due to the addition of noise to the data are shown for W = 0.1 (lower panel) as well as for W = 1 without weighting (upper panel). In both plots, the error curves from the noisy data are shown superimposed on the noise-free error curves (thin solid lines), and the errors shown are obtained based on a single realization and for a time domain $\Delta T = 7.6$ and $\Delta t = 0.2$. As before, vp denotes velocity projection, while da1 and da0 denote the assimilations that begin, respectively, from a linear initial velocity profile and from a state of rest.

[39] Figure 6 shows that the main effect of the data noise on the projection errors is to cause the errors to fluctuate irregularly about their previous level for the noise free data. This fluctuation is reduced substantially, however, in the case of W = 0.1. Similarly large reduction is found with other W values of similar magnitude, but the fluctuation becomes large again for an order of magnitude smaller W or $W < 0.01$. The fact that $W \sim 0.1$ yields the optimal result here is consistent with the expectation, namely, that when the constraints are appropriately weighted, the residual of the fit to data should have a variance comparable to the noise variance. This is confirmed for $W \sim 0.1$

[40] The forecast errors with continuous data assimilation can be seen to similarly benefit from the weighted data constraints. At this point, one can also view the inaccurate initial condition that starts the assimilative forecast as corrupted data and assign it (11f) a small weight that reflects the size of its uncertainty. For the linear initial profile, a weight of 0.01 is estimated. The resulting forecast based on this weight and W = 0.1 for the data does show a reduction in error, but the error level remains significant. Since decreasing the weight decreases the influence of initial condition in the assimilative forecast, continuous reduction of the weight is found simply to reduce the forecast errors toward the level of error in velocity projection as expected.

5.5. Variable Viscosity

[41] Any functional form of eddy viscosity can be incorporated into projection formalism by using the more general momentum diffusion term of the form shown in (1). The complication lies in the dependence of E on flow variables such as kinetic energy, shears, etc. This dependence renders the velocity projection nonlinear. One possible approach to dealing with this nonlinear problem is to begin with a guess viscosity and then iterate until the solution converges as attempted by *Shen and Evans* [2001]. The numerical simulation in section 4 with variable E_t provides a benchmark for testing this iterative approach. For this test, the right-hand side of (8a) or (11a) is multiplied by 1/r to account for the effect of variable eddy viscosity on current shear in the wind stress boundary condition. At the start of the iteration, the viscosity value is set to a constant for the entire ΔT domain and is estimated by using the time-averaged surface velocity in the eddy viscosity model. During the iteration the viscosity value for the first 1/2 of ΔT, however, is continually held fixed at the initial constant value, while E_t for the remaining 1/2 of ΔT is updated after each projection until a convergence in the viscosity value is reached; in other words, iteration is performed only in the later half of ΔT where the projection is expected to work well.

[42] Figure 7, upper and middle panels, show the errors (vp) between the projection and the benchmark case for the time domain $0 \le t_k \le 7.6$ at the end of five iterations, at which point E_t has converged. The error curves, immediately after $t_k = 7.6$, are those for the forecast with data assimilation that continues from the end of the projection; the integration time step for the forecast is $\Delta t = 0.2$, and the data is assimilated at each step. As before, the errors for the two forecasts (da0 and da1) starting from incorrect initial conditions at $t_k = 0$ but controlled with continuous assimilation of the same surface data are also plotted for comparison. Once again, for both the projection and data assimilation cases, the velocity errors can be seen to decrease in time toward a limiting value, and their angular errors approach zero. The errors, however, are more variable

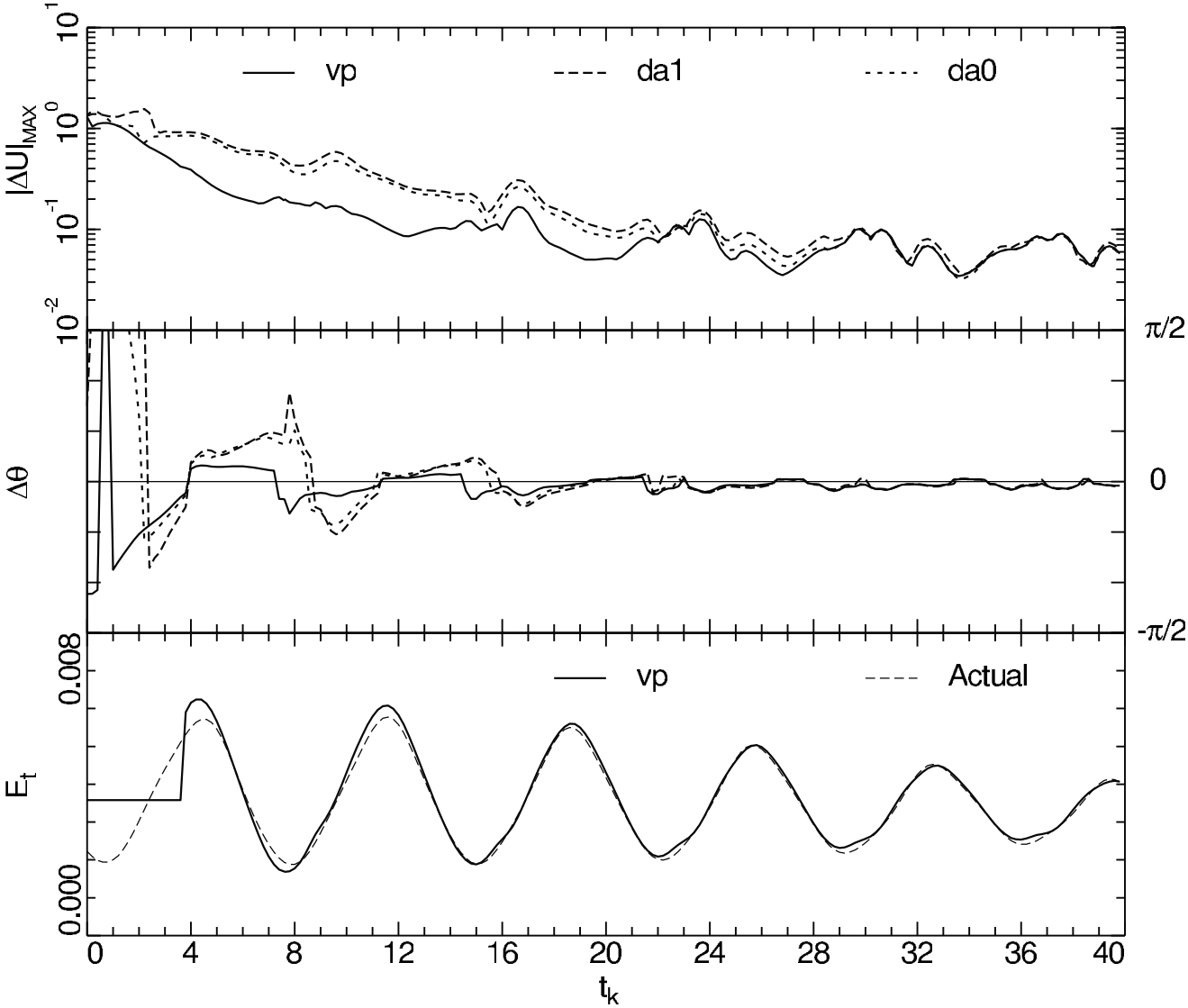

Figure 7. $|\Delta U|$ and $\Delta\theta$ errors for the variable eddy viscosity case, and the comparison of the estimated eddy viscosity parameter E_t to the actual one used in the benchmark case. The symbols vp, da1, and da0 are as in Figure 5.

than those for the constant eddy viscosity cases. The E_t value estimated from the projection and subsequent data assimilation forecast is shown as a function of time in Figure 7, lower panel. It is seen that despite holding E_t constant in the beginning, E_t estimated subsequently from the iteration follows closely the temporal variation of the actual E_t from the benchmark case.

5.6. Surface Height Gradients

[43] Once the current profiles have been estimated, the unknown tidal forcing given by the R term in the form of sea surface height gradients can be computed from (4b). Figure 8 illustrates the accuracy with which the two R components, R_x and R_y, can be obtained from (4b) in both the velocity projection (vp) and assimilation (da1). Figure 8a illustrates this for the constant E_o case and Figure 8b for the variable E_t case. In both cases, the velocity projection is done over the time domain $0 \leq t_k \leq 7.6$, and after which data assimilation is carried out using the current profile at the end of the projection as the initial condition, while da1 as before refers to data assimilation beginning at $t_k = 0$ from a linear initial current profile. The actual R_x and R_y used in the numerical simulations are plotted as thin solid curves in the figure. Except for the large deviation near the beginning, it is clear that the forcing function R can be recovered well using (4b), as R for both vp and da1 tracks closely the actual R in time. It is worth noting that the initially large difference between the estimated and actual R decreases rapidly with time; the estimated R converges to actual R in as little as a third tidal cycle, during which time the projection errors are still substantial (Figure 5). This indicates that R can be robustly estimated as part of the velocity projection.

6. Summary

[44] This study has presented a velocity projection approach that obtains estimates of subsurface current structure from surface current velocities in a manner consistent

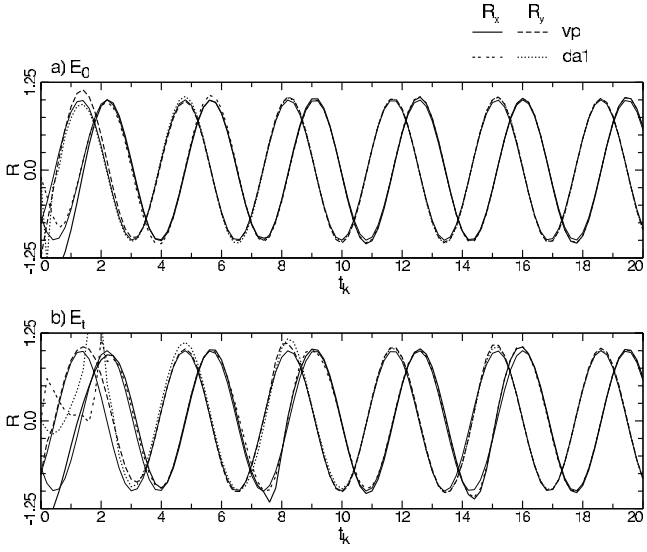

Figure 8. Comparison of the estimated tidal forcing R to the actual forcing (thin solid curves). (a) E_o, constant eddy viscosity case. (b) E_t, variable eddy viscosity case. The symbols vp and da1 are as in Figure 5.

with the interior current dynamics. The particular situation considered is the coastal current in well-mixed homogeneous water forced by winds and tides, and the current obeys the viscous shallow water dynamics. The current structure projected from the surface is thus required to satisfy the viscous shallow water momentum equations. This dynamic constraint and the surface velocity data constraint are then supplemented by the wind stress boundary condition at the sea surface and the no-slip velocity condition at the seabed; additionally, the sea surface slope which is difficult to measured is removed from the momentum equations by exploiting the viscous and pressure balance at the no-slip seabed. The velocity projection problem is reduced to one spatial (vertical) dimension by considering linearized shallow water dynamics with vertical dissipation, and the data and dynamic constraints are inverted directly for the subsurface current structure by the method of singular value decomposition. It is shown that an overdetermined system of constraints can be obtained for a discrete surface data time series whose length exceeds the number of vertical modes used to approximate the current profile.

[45] The velocity projection with linear dynamics clearly contains model errors, which must be dealt with in any least squares inverse solution by appropriately weighting the dynamic constraints, as noted in the introduction section. However, in order to fully understand and assess the capabilities and limitations of the method, the model physics in this study has been treated as perfect and used to generate simulated data and current profiles, and then the accuracy and sensitivity of the method are tested against the simulated results by this twin-experiment approach. It is shown that the length of the time domain is as important as the size of the projection time step in determining the projection accuracy. At minimum, the time domain needs to span the dominant period of current oscillation while the time step resolves this oscillation. When both are achieved, the estimated current profiles converge to the simulated true profiles. The dependence of the solution accuracy on time domain is shown to be also inherent in the assimilative forecast calculation that begins from an inaccurately known initial condition. However, the approach to convergence can be slower than velocity projection.

[46] The sensitivity of projection results to noise has been tested by randomly perturbing the simulated surface current data and wind stress data. The projection method is shown to be robust, and with appropriate weighting of the data constraints, the effect of noise on the solution accuracy can be minimized. For the assimilative forecast calculation, the inaccurate initial condition can also be thought of as noisy data and weighted similarly. Although this leads to improved forecast solution, it still lags behind velocity projection, unless the initial condition is given a negligible weight, in which case the accuracy becomes comparable.

[47] The velocity projection obtains the sea surface slope as part of the subsurface current estimation. The estimated sea surface slope is shown to be robust, and the estimate converges to the true (simulated) value more rapidly than the velocity estimate itself. The velocity projection can also account for spatially and temporally varying eddy viscosity and obtain estimates of the viscosity. However, this can not be done easily, as the eddy viscosity is often a function of the flow velocity to be estimated, which renders the projection problem nonlinear. An iterative approach has been illustrated in this study which yields eddy viscosity values consistent with the estimated current profiles.

[48] The actual ocean conditions are obviously much more complex than those simulated with the present homogeneous viscous shallow water model. There will be model errors arising from the neglect of nonlinear advection, the particular choice of eddy viscosity, and the specification of seabed boundary conditions, even when the assumed uniform density condition is valid for the region analyzed. It should be possible to reduce the effect of such model errors by giving smaller weights to the model dynamics, and to further controlled the errors by applying data constraints at all projection time steps; such a dense surface data coverage is presently available from the HF radar measurements. Thus, any application of the present method to actual field data will require at least a careful assessment of all the possible model errors, in addition to the data errors, namely, those of the surface velocity and wind stress, and then the weights must be chosen accordingly as discussed, for example, by *Wunsch* [1996].

[49] Although the true usefulness of the present velocity projection method can only be tested through its application to observations, certain implications of the present work for field applications, whether hindcasting coastal currents using historical data or nowcasting/forecasting with real-time data, already appear to be clear: (1) Unless the initial current profile is known a priori, inaccurate first guess tends to delay the convergence of the time-dependent solution, and the projection approach can allow a speed up by omitting the initial guess. (2) Because the early time solution depends partly on backward time integration of the solution at later times, it is not possible to obtain current profiles near the beginning of the analysis period without large errors, regardless of the temporal resolution and span of the surface observations. (3) Consideration must be given

to the number of vertical modes needed to approximate the profiles, which is both a function of the ratio of Ekman boundary layer depth to water depth and a function of the forcing frequency; typically, smaller the ratio or higher the forcing frequency more vertical modes are needed, as these conditions favor the presence of short vertically varying inertial oscillations. And, in turn, (4) the number of modes has a bearing on the minimum number of data needed to estimate the subsurface current profile as discussed in section 2

[50] The present study using nine vertical modes assumes a mid shelf condition with maximum forcing frequencies representative of the semidiurnal tide and diurnal onshore-offshore sea breeze. In practice, other conditions may be encountered such as a deeper shelf or the presence of a rapidly moving wind front; in these cases more vertical modes will be needed, and the number of surface data must be correspondingly increased for the estimation of the current profiles. At present, it appears that the suitable choice of vertical resolution will depend on the situation, and the adequacy of the vertical modal approximation can be verified only through some type of sensitivity tests such as the ones illustrated in this paper. Whether a desirable vertical resolution can be inferred from the observed surface current and wind variability is presently under investigation, as well as the extent to which velocity projection can be usefully applied to the real ocean situation.

Appendix A

[51] For each of the three cases shown in Figure 3, the extent of data dependence and solution dependence can be made apparent by computing the data resolution matrix, ***DD****, and the solution resolution matrix, ***SS****, respectively, where ***D*** is the complex matrix whose columns are the singular vectors that span the data vector, and ***S*** is the complex matrix whose columns are the singular vectors that span the solution vector; the asterisk denotes conjugate transpose. The dimensions of ***D*** and ***S*** for Figures 3a and 3b are both KNP $\times$ P, where P is less than KN and equals to the number of the nonsingular values above the cutoff, and for Figure 3c are, respectively, KNP $\times$ P and [N(K $-$ 1) + (K + 2)] $\times$ P. The solution vector $\tilde{\mathbf{a}}$, whose elements are the least squares solution $\alpha_j^{(k)}$, is related to the exact theoretical solution vector **a** by $\tilde{\mathbf{a}} = \boldsymbol{SS}^*\mathbf{a}$. The substitution of $\tilde{\mathbf{a}}$ into the left-hand side of the constraints yields the data vector estimate $\tilde{\mathbf{b}}$, which is related to the actual data vector **b** by $\tilde{\mathbf{b}} = \boldsymbol{DD}^*\mathbf{b}$. A data vector that fully resolves the flow thus will have $\boldsymbol{DD}^* = \mathbf{I}$ the identity matrix, and hence fully independent data vector components. When some diagonal elements in ***DD**** are less than unity, the corresponding data vector components are not independent. The same interpretation applies to ***SS****.

[52] Figure 9a (upper panel) is a plot of the diagonal elements, $D_{jj} = \mathrm{Real}(\boldsymbol{DD}^*)_{jj}$, for the $\Delta T = 1.2$ and $\Delta t = 0.2$ case. The ordering of the index is as follows: surface velocity data, j = 1 to 7; surface wind stress, j = 8 to 14; no slip bottom boundary conditions, j = 15 to 21, and dynamical constraints for the whole period, j = 22 to 63. The general lack of data independence is evident for this small ΔT case, consistent with the large projection errors found for this case. The portion pertaining to the surface

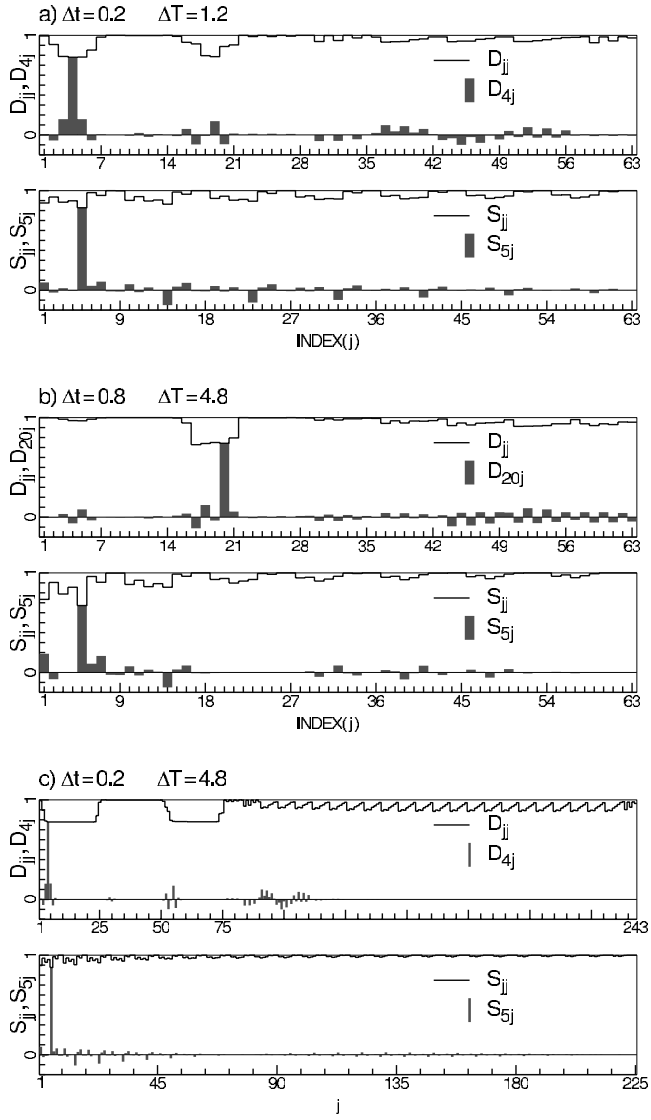

Figure 9. Elements of the data resolution matrix, ***DD****, and the solution resolution matrix, ***SS****, for the corresponding cases in Figure 3, where ***D*** and ***S*** are the singular vector matrices for the data vector and the solution vector, respectively.

velocity data, however, is of interest here. The nature of the data dependence in this region may be illustrated with a plot of the values of the row elements D_{4j}, shown by vertical bars in Figure 9a. It is seen that $\tilde{b}_4 = \sum D_{4j} b_j$ is a weighted linear combination of data at j = 2 to 6 as well as data at larger j indices; however, since $b_j = 0$ at the larger indices, the combination that yields $\tilde{b}_4$ reflects primarily the lack of independence of the surface velocity data. In Figure 9b for $\Delta T = 4.8$ and $\Delta t = 0.8$, the same diagonal elements related to the surface velocity data have nearly unity value, indicating the data sampled at larger Δt tend to be linearly independent. In Figure 9c, where ΔT with $\Delta t = 0.2$ have been increased to 4.8, matching the time domain size of the large Δt case, no significant change is seen in the values of the diagonal elements of the resolution matrix. But, as noted earlier, the solution accuracy is greatly improved with the

larger ΔT. Part of the reason for the improvement may be gleaned from the solution resolution matrix, $\boldsymbol{SS}^*$.

[53] In Figure 9c, lower panel, the diagonal elements of this resolution matrix, specifically, its real part $S_{jj} = \text{Real}(\boldsymbol{SS}^*)_{jj}$, are plotted in the order of ascending modes for successive times, that is, j = 1 to 9 for $\alpha_n^{(1)}$ with n = 0, 1, 2,. . ., 8, then j = 10 to 18 for $\alpha_n^{(2)}$, etc. The plot shows S_{jj} near the beginning of the projection time domain (small j's) has values less than unity and approaches unity near the end of the domain (large j's). This means that with the extended ΔT, the solution $\alpha_n^{(k)}$ at later times is increasingly less affected by or less dependent on earlier $\alpha_n^{(k)}$. In view of this result, it is of interest to reexamine D_{4j} plot for the data dependence indicated previously by $D_{jj} < 1$ between j = 4 and j = 22 in Figure 9c, upper panel. The illustrative D_{4j} plot (vertical bars) shows that the range of dependence for the surface velocity data, in the present case at j = 4, is limited to the immediate vicinity of the diagonal element D_{44}. Evidently, for large ΔT, the data dependence being of limited range cannot have an effect on $\alpha_n^{(k)}$ separated far in time. In a sense, large ΔT reduces the interdependence of velocity data obtained at small Δt, and consequently, the projection accuracy should improve.

[54] In Figure 3, the projection near the beginning of the time domain is consistently poor irrespective of the sizes of ΔT and Δt. The plots of S_{5j} in Figure 9 for the three cases illustrate that the solutions at early times (small j) invariably depend on the solutions at the later times; specifically, at j = 5, $S_{55} < 1$, $\tilde{a}_5 = \sum S_{5j} a_j$, and $S_{5j} \neq 0$ for some $j \neq 5$. For the forced-dissipative flow considered here, velocity information at early times is invariably lost as flow evolves. Since the dependence of the early time solution on the later time solution is tantamount to reverse time integration, the projection method can not accurately recover the early time solution in this case.

[55] **Acknowledgments.** This work is a contribution to the Optimal 3D Currents Form Remote Scene Sequences project, 72-7815, at the Naval Research Laboratory, sponsored by the Office of Naval Research.

References

Lanzcos, C., *Applied Analysis*, Prentice-Hall, Old Tappan, N. J., 1956.

Lewis, J. K., I. Shulman, and A. F. Blumberg, Assimilation of Doppler radar current data into numerical ocean models, *Cont. Shelf Res.*, *18*, 541–559, 1998.

Paduan, J. D., and L. K. Rosenfeld, Remotely sensed surface currents in Monterey Bay from shore based HF radar (CODAR), *J. Geophys. Res.*, *101*, 20,669–20,686, 1996.

Prandle, D., A new view on near shore dynamics based on observations from H.F. radar, *Prog. Oceanogr.*, *27*, 403–438, 1991.

Scott, R. K., J. S. Allen, G. D. Egbert, and R. N. Miller, Assimilation of surface current measurements in a coastal ocean model, *J. Phys. Oceanogr.*, *30*, 2359–2378, 2000.

Shay, L. K., H. C. Graber, D. B. Ross, and R. D. Chapman, Mesoscale ocean surface current structure detected by HF radar, *J. Atmos. Oceanic Technol.*, *12*(4), 881–900, 1995.

Shen, C. Y., and T. E. Evans, Surface-to-subsurface velocity projection for shallow water currents, *J. Geophys. Res.*, *106*, 6973–6984, 2001.

Wunsch, C., Using data with models: Ill posed problems, in *Oceanographic and Geophysical Tomography*, edited by Y. Desaubies, A. Tarantola, and J. Zinn-Justin, 205–248, North-Holland, New York, 1990.

Wunsch, C., *The Ocean Circulation Inverse Problem*, Cambridge Univ. Press, New York, 1996.

T. E. Evans and C. Y. Shen, Code 7250, Remote Sensing Division, Naval Research Laboratory, Washington, DC 20375, USA. (shen@ccf.nrl.navy.mil)